Electrical Power and Energy Systems 115 (2020) 105514

Contents lists available at ScienceDirect

Electrical Power and Energy Systems

journal homepage: www.elsevier.com/locate/ijepes

A magnetic loop antenna for partial discharge measurements on GIS

A. Rodrigo Mor*, L.C. Castro Heredia, F.A. Muñoz

Delft University of Technology, Electrical Sustainable Energy Department, Delft, the Netherlands

ARTICLE INFO

Keywords:
Partial discharge
GIS
Magnetic sensor
Magnetic loop antenna
Charge calibration

ABSTRACT

This paper presents a magnetic loop antenna for partial discharge (PD) measurements on gas insulated systems (GIS). The antenna is based on a single shielded loop inserted in the dielectric window of a GIS that measures the PD currents propagating in TEM mode. The paper describes the relevant parameters of the antenna and the antenna performance in combination with a transimpedance amplifier. A calibration method for charge estimation is presented along with laboratory experiments with free moving particle, surface and corona discharges in SF_6 test cells. The results show the suitability of the magnetic antenna for PD detection and the charge evaluation performance. Under laboratory conditions, the antenna sensitivity is in the order of 1 pC at a few meters from the PD source.

1. Introduction

Partial discharge measurements in GIS are commonly performed using the ultra-high frequency (UHF) method. The high sensitivity of the UHF method and its high resilience to electromagnetic interference (EMI) has consolidated its application as a standard for on-line monitoring of GIS installations. However, some concerns still lay on the fact that the return of investment can be only justified for critical installations with high outage costs [1].

Recently, HVDC GIS technology is being taken under consideration mainly for offshore substations. The lack of return of experience from DC GIS operation can be decisive for further developments of PD techniques. The brochure of the CIGRE JWG D1/B3.57 (brochure still in progress), in fact, retains the recommendation of PD testing (pre-qualification tests) and backs the development of time sequence analysis techniques, such as the "NoDI*" [2] patterns, specifically applied for DC GIS/GIL systems.

Although the time sequence analysis is common in laboratory studies with small test objects, no attempts have been reported aiming to its application on actual GIS. This, partly because the calibration to apparent charge is not possible from UHF measurements. Charge estimation might require time domain acquisition of PD signals with wide bandwidths, which hasn't piqued the interest of researchers due to the noise and EMI problems that entail broadening the measuring bandwidth. In addition, in HV equipment under DC electric fields, PD pulses may occur in bursts quite far apart in time [23], raising even more the concerns around noise and disturbances acquisition over time.

However, nowadays a plurality of post-processing techniques aided by clustering and machine learning algorithms have become available. Hence the recognition of real PD from noise/disturbances should increase its chances of success. Studies such as that in [4], among many more, reportedly managed to identify PD sources in presence of disturbances, resorting for instance to the *TW* classification map.

This investigation also focuses on the time domain acquisition of signals from an actual size GIS with the particularity that the detection of the PD signals is achieved via magnetic sensors that measure the surface currents created by the PD events and that flow along the GIS compartments. The sensor is designed to work mainly in the high frequency range (HF) and extending towards the lower end of the very high frequency range (VHF), which implies that all the measurement results reported in this paper concern to the TEM propagation mode of the PD signals.

In previous contributions from the authors this concept of magnetic detection in the HF range proved feasible for PD detection [5] and in turn, in [6] we demonstrated that the surface currents of the TEM propagation mode have a homogeneous current distribution in the GIS compartment perimeter, which opened the possibilities for further research on PD quantification.

In the present contribution, the sensitivity of the magnetic sensor is boosted by using current amplification unlike the voltage amplification of the sensor output reported in [5]. In addition, a test-bench frequency characterization of the new design of the magnetic sensor is presented. Next, the results of a calibration procedure in terms of pC are shown. The sensitivity of the proposed antenna is studied in laboratory conditions using free moving particle, surface and corona discharges produced in test cells in SF_6. Finally, this paper discusses the ability of this

* Corresponding author.
E-mail address: A.RodrigoMor@tudelft.nl (A. Rodrigo Mor).

https://doi.org/10.1016/j.ijepes.2019.105514
Received 26 June 2019; Received in revised form 16 August 2019; Accepted 23 August 2019
Available online 28 August 2019

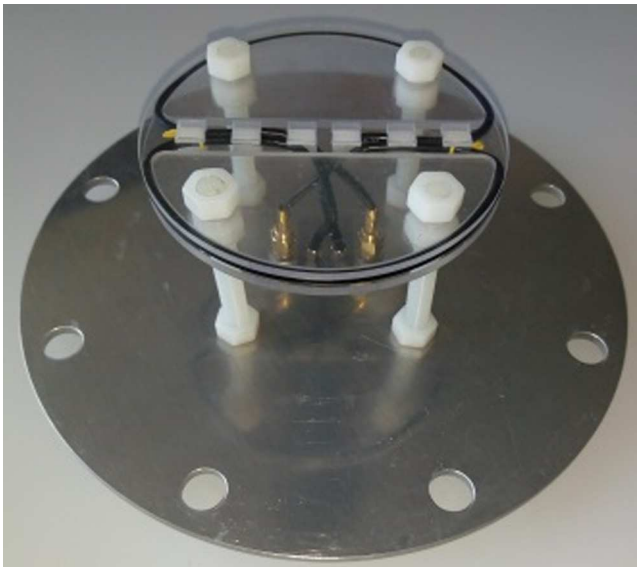

Fig. 1. Construction of the magnetic antenna showing both 1-turn loops assembled on the mounting plate.

approach for PD detection and limitations in charge estimation.

2. Magnetic antenna for PD detection on GIS

The principles of how a PD event creates surface currents that travel along the GIS compartments have been presented in [5,6]. In [5], a magnetic shielded-loop antenna using five turns and a high input impedance voltage amplifier was presented. In that case, due to the high input impedance of the amplifier, the resonance of the antenna was determined by the loop inductance and the parasitic capacitance of the shielding. This combination created a resonance peak around 32 MHz and oscillatory waveforms because the underdamped response of the system.

To overcome the bandwidth problem and reduce the signal oscillations, a new magnetic antenna consisting of a single shielded loop in combination with a low input impedance transimpedance amplifier is proposed in this work.

The antenna consists of two shielded loops made out of RG179 coaxial cable to provide shielding. Each loop has a half circle shape, see Fig. 1, with an inductance of 218 nH and 32 pF capacitance from the coaxial cable. The antenna diameter is 103 mm and the distance to the mounting plate is 53 mm.

The antenna distance to the mounting plate is such that the antenna perimeter levels the edge of the internal wall of dielectric window with the internal GIS enclosure. The antenna diameter has been chosen to have a 2 mm clearance to the inner walls of the dielectric window. This clearance is due to mechanical reasons. It is necessary for the antenna installation to overcome the internal bump produced by the perimeter welding of the window pipe to the GIS compartment. Schematic views of the antenna installation in a GIS are shown in Fig. 2.

As presented in [5], the magnetic antenna has two loops, (top and bottom) that pick up the magnetic field produced by the PD currents surrounding the opening of the dielectric window in the enclosure. Each loop is connected in such a way that the inner loop formed by the inner coaxial cable conductor forms the measuring loop and is connected to the amplifier, whereas the outer loop formed by the coaxial cable screen is only grounded in one side and left floating in the other. The screen connection is done in this way to provide electrostatic shielding and to prevent short-loop currents that will counteract the external magnetic field detected by the magnetic antenna.

The electric equivalent circuit of the loops is shown in Fig. 3. *Ra1i* and *Ra1o* represent the inner and the screen coaxial cable resistance.

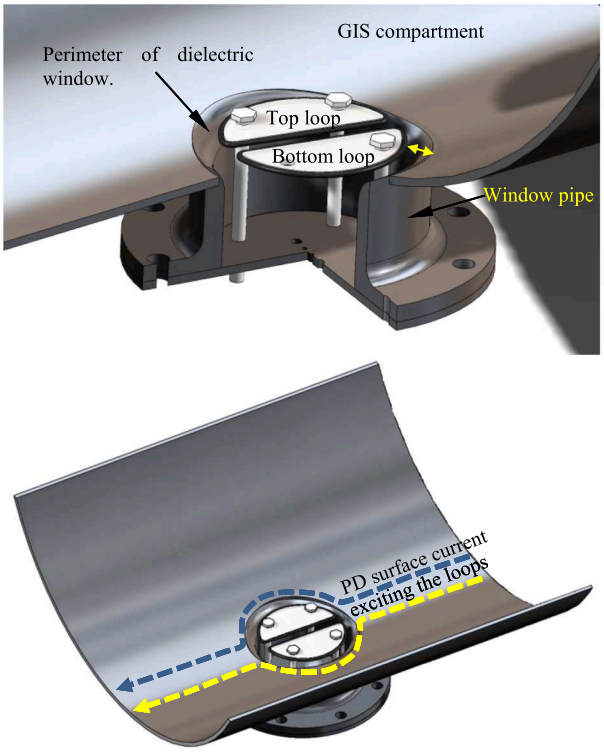

Fig. 2. Intersection of the GIS compartment and the dielectric pipe that results in a window in the GIS compartment. (a) Cutaway view of the position of the magnetic antenna relative to the compartment window; (b) perspective view of the PD current around the magnetic antenna.

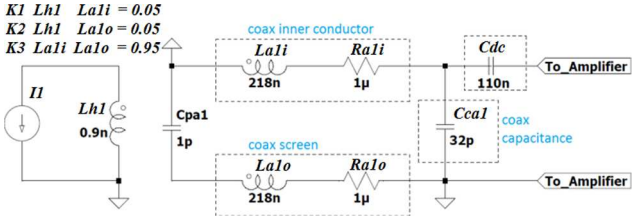

Fig. 3. Equivalent electric circuit of the magnetic antenna.

La1i and *La1o* accounts for the inner cable and screen inductance, whereas *Cca1* is the loop capacitance due to the coaxial cable capacitance. *Cpa1* accounts for the parasitic capacitance of the floating end screen. *Lh1* is the inductance of the hole in the GIS dielectric window. *Lh1* is calculated as the flux created in half dielectric window per amp flowing in the GIS. *Lh1* and the coupling coefficients *K1*, *K2* and *K3* have been calculated via simulations using electromagnetic finite element simulations.

The magnetic antenna is loaded with a commercially available transimpedance amplifier model Femto HCA-40M-100K-C. A parallel $2 \times 0.056\,\mu F \pm 10\%$ ceramic decoupling capacitor, *Cdc*, has been connected in series between the antenna and the transimpedance amplifier to block the DC coupling. Otherwise, the DC feedback loop of the transimpedance amplifier has zero resistance and the electronics goes to saturation. The complete arrangement connection is depicted in Figs. 4 and 5.

3. Antenna characterization

A calibration rig was built to test the performance of the magnetic antenna and its associated electronics.

The calibration rig, shown in Fig. 5, has the same dielectric window size and compartment's internal diameter than the full-scale testing GIS

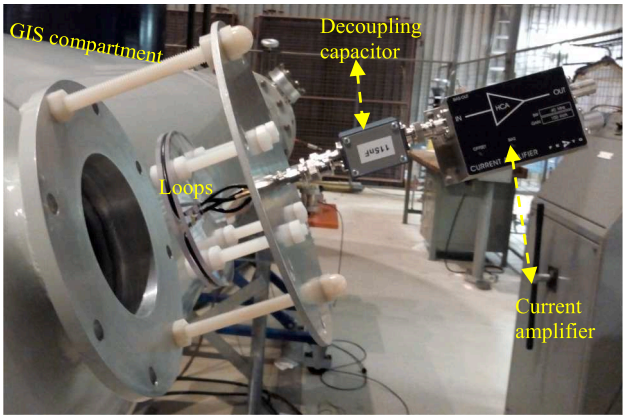

Fig. 4. Connection arrangement of the magnetic antenna, decoupling capacitor and transimpedance amplifier.

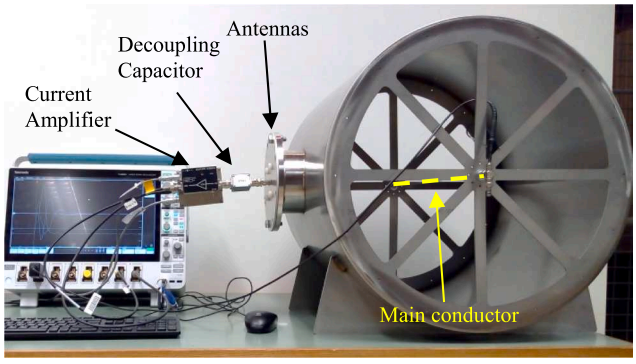

Fig. 5. Calibration rig workbench.

available at the High Voltage Laboratory of Delft University of Technology. Since the relevant dimensions of the calibration rig and the actual GIS are the same, the current distribution in both enclosures is the same. Therefore, the calibration rig can be used to characterize the behavior of the antenna in the GIS.

The calibration rig consists of a nonmagnetic stainless-steel tube, 1 m long and 3 mm thick, with a dielectric window in the middle. Each end of the tube continues in a flat-spoke structure with BNC connectors at the center. The central conductor is a wire with a 1 mm diameter through a high frequency transformer (HFCT), model FCT-016-5.0 from Bergoz with 3.92 kHz–1.11 GHz bandwidth, that measures the flowing current in the tube. The calibrator signals are injected in one BNC, while the other is terminated with 50 Ω. The signal from the HFCT triggers the simultaneous acquisition of the HFCT and antenna signals by the oscilloscope.

Fig. 6 shows a calibrator pulse, measured by the HFCT, and the measured signal in one of the magnetic antenna coils. By using the spectrums of both signals is possible to derive the frequency response of the magnetic antenna. The estimated Bode diagram of the antenna is depicted in Fig. 7.

The frequency response of the antenna has been obtained with the configuration explained in chapter 2. It shows the relationship between the measured voltage and the total propagating current in TEM mode in a GIS enclosure.

It is worth to notice that:

- The frequency peak is around 52 MHz which is an improvement with respect to the magnetic antenna presented in [5].
- The PD current flows with a homogeneous current distribution along the GIS compartments, but only the part that surrounds the dielectric window induces significant EMF in the loops. The combination antenna-electronics has gain enough as to boost the sensitivity of the antenna.
- The phase diagram shows that although the antenna is loaded with a low input impedance amplifier, the antenna still shows a derivative behavior in the low frequency range.
- There is energy content in the HF range, in opposition to the traditional VHF and UHF antennas.

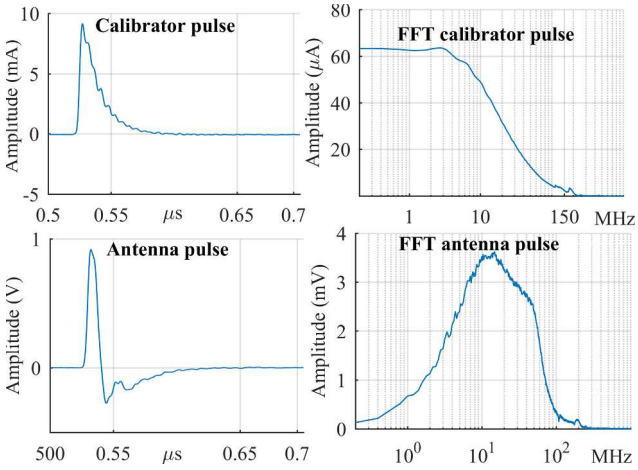

Fig. 6. Magnetic antenna response to a calibrator pulse.

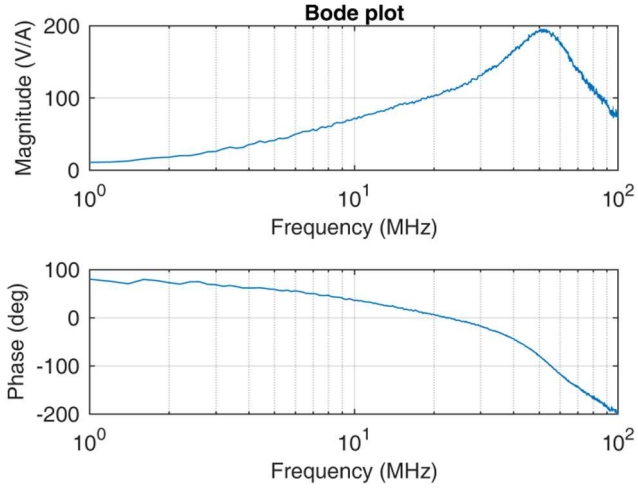

Fig. 7. Bode diagram of the magnetic loop antenna.

4. Charge calibration

In [6], it was experimentally demonstrated that the PD currents flowing along the GIS compartments have a homogeneous current distribution in the compartment's perimeter. An important implication of this finding is that the total PD current flowing along the compartment and the antenna's output can be correlated. Therefore, by means of a calibration factor, the measured signals can be related to the input charge.

In order to test this concept and to obtain the calibration factor the following procedure was conducted:

(1) Signals from a pulse calibrator were injected in the calibration rig and measured with the HFCT.
(2) The charge of the injected pulse was calculated as the integral of the current signal following the procedure in [7,8].
(3) The cumulative integral $I(n)$ of the antenna's output $v(n)$ was computed according to Eq. (1).

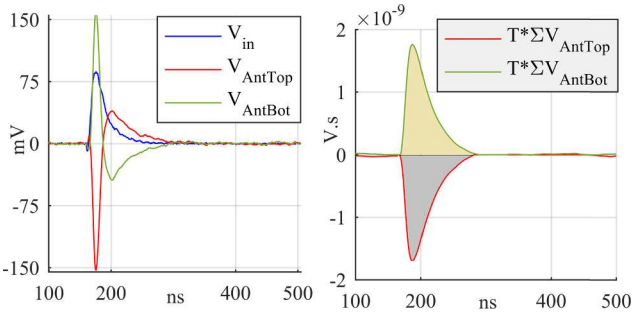

Fig. 8. Left: example of injection of a 50 pC pulse and response from the antennas; right: integration of the antenna's output.

$$I(n) = \frac{1}{F_s}\sum_{1}^{N} v(n) \tag{1}$$

where $1/Fs = T$ is the time step or sampling period. Note that I(n) is not a current signal, but it has units of [V·s] instead.

(4) Finally, the integration between the zero-crossings of the main peak of I(n) was calculated as indicated by the shaded areas in Fig. 8. From a mathematical point of view, this procedure is a double time integral calculation of the antenna signal.

Because both loops are in a mirror-like arrangement, the polarity of the output signals from the loops are opposite to each other. Likewise, the charge carries the polarity of the signal from which it was computed.

The results of this procedure are plotted in Fig. 9. In this graph, the y-axis corresponds to the injected charges, ranging from 5 pC to 500 pC, and the x-axis corresponds to the value of the double time integral of the signal from the antennas.

After curve-fitting these results, a calibration factor K_c was calculated.

$$K_c = 7.1862 \times 10^5 \left[\frac{C}{V{\cdot}s^2}\right]$$

5. PD detection and sensitivity

The ability of the new design of the magnetic antenna to detect PD signals was tested in a 380 kV AC GIS. In Fig. 10, it can be observed that at one end, the GIS was given a structure so that a test cell could be placed axially with the main conductor. An HFCT was inserted right next to the test cell to measure the PD current at its source and the magnetic antenna was installed 3.3 m away from the test cell. Testing voltages, test cells and other parameters related to the measurement

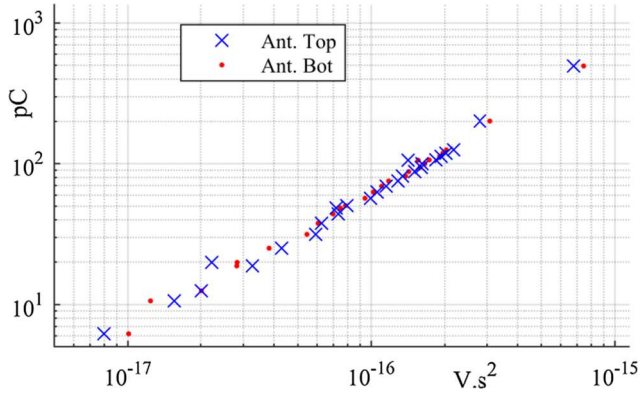

Fig. 9. Relation between the injected charge and the integral response from the antennas tested in the test bench.

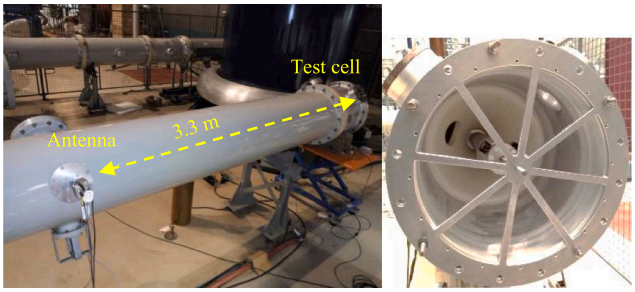

Fig. 10. Localization of the magnetic antenna and test cell in the GIS.

Table 1
Testing and sensor parameters.

	Corona	Surface	Free particle
AC test voltage	15 kV	22 kV	12 kV
SF_6	1 Bar	1.2 Bar	2 Bar
Test cell HFCT	Gain 9.1 mV/mA, BW 62 kHz–136 MHz		
HFCT Amplifier	25.5 dB, 23 kHz–1.14 GHz		–

set-up are summarized in Table 1.

The three signals (top/bottom antenna and test cell HFCT) were simultaneously sampled by an oscilloscope where the trigger source was set to one of the channels corresponding to the magnetic antenna. For each of the three tests, 1000 trigger events were acquired at a sampling rate of 1.25 GSa/s and saved for post-processing.

The main purpose of these tests was to validate that the magnetic antenna suitably responded to PD signals and check the minimum charge detection level.

One first validation of the correct functioning of the antenna came out of the good matching of the PRPD pattern obtained from the antenna and the one obtained from the test cell HFCT. In Fig. 11–13, the phase resolved partial discharge (PRPD) patterns of the top magnetic loop and the HFCT in the test cell are shown. Note that the polarity of the pattern from the magnetic antenna is reversed compared to that of the HFCT. That is because of the polarity of the HFCT with respect to the top magnetic loop polarity.

In addition, the waveforms from the antenna and from the HFCT, corresponding to the same trigger event, are compared. A signal from the antenna was considered as a true PD signal only if the corresponding signal from the HFCT had a reference waveform. This visual validation of the signals was assisted by the tool *PDflex* [9].

Figs. 14–16 show an example of a discharge from each of the test cells.

For all the three PD tests, the PRPD patterns and the visual validation of the waveforms confirmed that the antenna properly detected the PD signals created by the test cells.

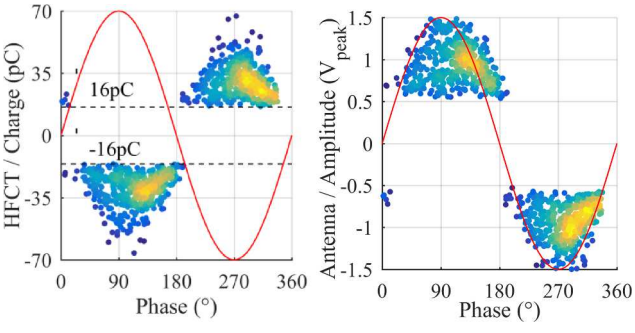

Fig. 11. PRPD pattern of free moving particle. Left: test cell HFCT; right: top loop.

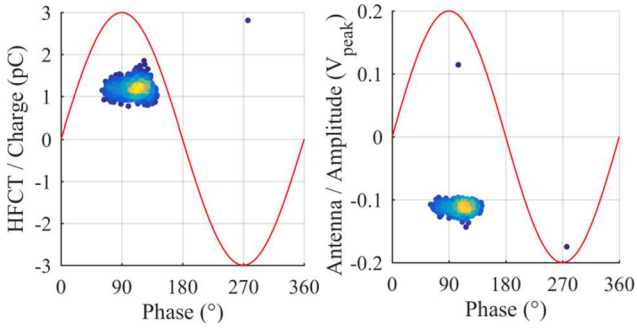

Fig. 12. PRPD pattern of corona. Left: test cell HFCT; right: top loop.

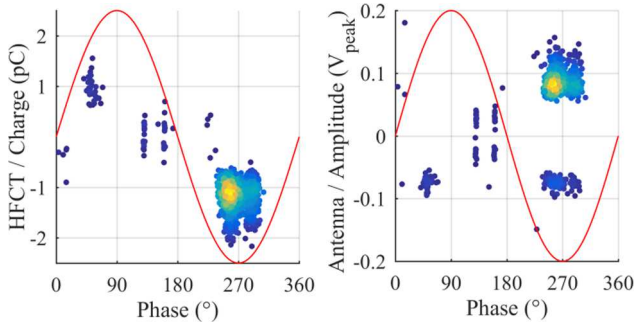

Fig. 13. PRPD pattern of surface discharges. Left: test cell HFCT; right: top loop.

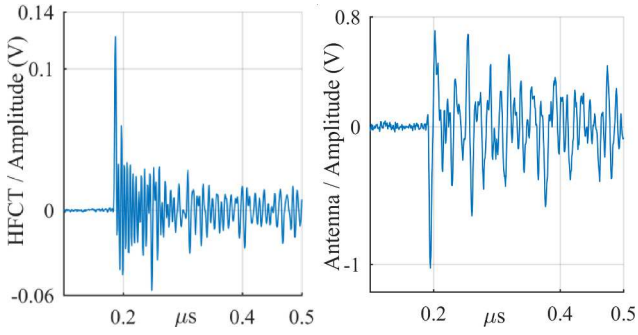

Fig. 14. Free moving particle signal. left: test cell HFCT; right: magnetic antenna.

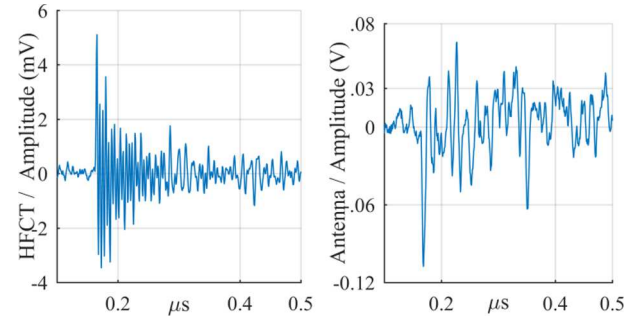

Fig. 15. Corona signal. left: test cell HFCT; right: magnetic antenna.

6. Charge estimation

After the measurement, the described charge estimation method based on the double time integral was applied to the free moving particle measurement.

The procedure is rather straightforward: The integration method described in chapter 4 is applied to the signals from the antenna and the results are translated into charge values by the calibration factor.

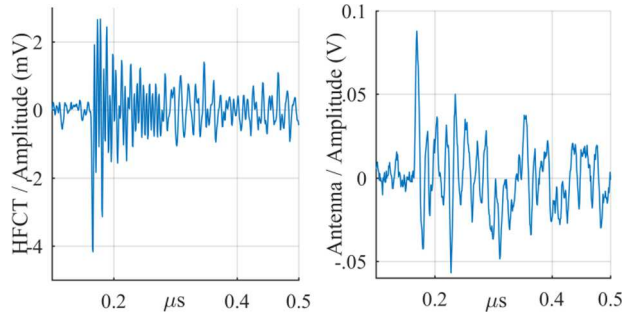

Fig. 16. Surface discharge signal. left: test cell HFCT; right: magnetic antenna.

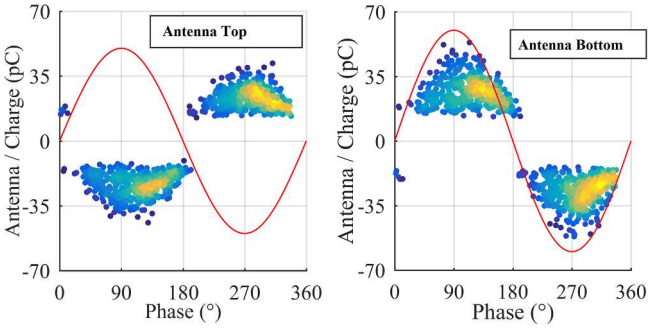

Fig. 17. PRPD of free moving particle test measured by left: top antenna, right: bottom antenna.

Fig. 17., displays the PRPD patterns from the bottom and top antenna that correspond to the translation to pC of the Fig. 11 left side.

The comparison of both patterns shows that the charge estimated from the antenna correlates to the charge measured at the test cell, Fig. 11 left side, hence the shape of the patterns also matched.

The goodness of the correlation is illustrated in Fig. 18 where the pC from the test cell HFCT are related to the pC calculated from the antennas. Two remarks can be inferred from the results. The first one concerns the alignment differences in both antennas that lead to a better correlation of results from the bottom antenna. The second one is

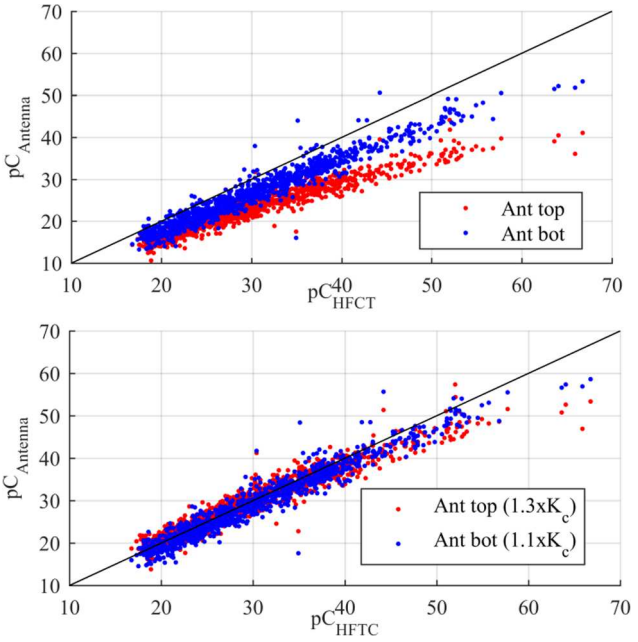

Fig. 18. Top: correlation between the charge values from the test cell HFCT and the antennas; bottom: compensation of the calibration factor.

that a compensation of 10% and 30% for the results from the bottom and top antenna respectively corrects the deviation as illustrated in Fig. 18 bottom side.

The charge estimation was difficult to perform in the corona and surface discharge tests, although the PD signals were properly detected despite of the their low amplitude. For these PD sources the peak amplitude of the antenna output decreased almost ten times compared to the case for the free moving particle test. With such small signals, the amplitude of the main peak and the peaks due to the pulse reflection are comparable. After integration, the peak due to the PD pulse is difficult to detect and therefore so are the integration limits, which in turn jeopardizes the charge estimation.

7. Conclusion

The research presented in this paper shows that a single turn magnetic loop antenna in combination with a transimpedance amplifier is a feasible option for partial discharge measurements on GIS.

The antenna characteristics have been presented along with its frequency response. A calibration rig has been used to characterize the magnetic loop antenna and to obtain a calibration constant. The calibration constant relates the double time integral value of the antenna signal to the charge of the input current.

Experimental results with free moving particle, corona and surface discharges, all in SF_6 gas, have proven that the magnetic loop antenna is able to detect small discharges, in the order of 1 pC at 3.3 m distance from the source. Furthermore, it has been possible to apply charge estimation methods in the free moving particle test using the double integral method. The results showed a good correlation between the estimated charge values and the charge measured at the test cell.

However, it was not possible to estimate the charge value of the measurements of corona and surface discharges due to their very low amplitude that made it difficult to detect the integration limits needed for the calculation. Further developments related to signal post processing techniques or antenna signal to noise ratio performance are needed to overcome this limitation.

Declaration of Competing Interest

The authors declared that there is no conflict of interest.

Acknowledgment

This project has received funding from the European Union's Horizon 2020 research and innovation programme under grant agreement No. 691714.

References

[1] H.-D. Schlemper, U. Riechert, G. Behrmann J. Manz, Application and benefits of UHF on-line partial discharge monitoring in GIS, CIGRÉ colloquium study committees A3, B4 & D1, Winnipeg; 2017.

[2] Pirker A, Schichler U. Partial discharge measurement at DC voltage — Evaluation and characterization by NoDi∗ pattern. IEEE Trans Dielectr Electr Insul June 2018;25(3):883–91.

[3] Judd M, Siew WH, Hu X, Corr E, Zhu M, Reid A, et al. Partial discharges under HVDC conditions, euro techcon, stratford-upon-avon, UK; December 2015.

[4] Cavallini A, Montanari GC, Tozzi M, Chen X. Diagnostic of HVDC systems using partial discharges. IEEE Trans Dielectr Electr Insul 2011;18(1):275–84.

[5] Rodrigo Mor A, Muñoz FA, Castro Heredia LC. A novel antenna for partial discharge measurements in GIS based on magnetic field detection. Sensors 2019;19(4).

[6] Rodrigo Mor A, Castro Heredia LC, Muñoz FA. A novel approach for partial discharge measurements on GIS using HFCT sensors. Sensors 2018;18(12).

[7] Mor AR, Heredia LCC, Muñoz FA. Estimation of charge, energy and polarity of noisy partial discharge pulses. IEEE Trans Dielectr Electr Insul 2017;24(4):2511–21.

[8] Mor AR, Morshuis PHF, Smit JJ. Comparison of charge estimation methods in partial discharge cable measurements. IEEE Trans Dielectr Electr Insul April 2015;22(2):657–64.

[9] TUDelft. Unconventional partial discharge analysis. Available online: http://pdflex.tudelft.nl [accessed on 28 January 2019].

Armando Rodrigo Mor (M'14) is an Industrial Engineer from Universitat Politècnica de València, in Valencia, Spain, with a Ph.D. degree from this university in electrical engineering. During many years he has been working at the High Voltage Laboratory and Plasma Arc Laboratory of the Instituto de Tecnología Eléctrica in Valencia, Spain. Since 2013 he is an Assistant Professor in the Electrical Sustainable Energy Department at Delft University of Technology, in Delft, The Netherlands. His research interests include monitoring and diagnostic, sensors for high voltage applications, high voltage engineering, and HVDC.

Luis Carlos Castro was born in Cali, Colombia in 1986. He received the Bachelor and PhD degree in electrical engineering from Universidad del Valle, Cali, in 2009 and 2015 respectively. Currently, he is a post-doc in the Electrical Sustainable Energy Department at Delft University of Technology, in Delft, The Netherlands. His research interests include high-voltage technology, partial discharge testing, accelerated aging of stator insulation and monitoring and diagnostic tests.

Fabio Andrés Muñoz was born in Cali, Colombia, in 1988. He received the B.S. degree in electrical engineering from the Universidad del Valle, Cali, in 2011, and PhD degree in 2017 from the same university. Currently, he is a post-doc in the Electrical Sustainable Energy Department at Delft University of Technology, in Delft, The Netherlands. His main research interests are focused on high voltage engineering, insulation diagnostics and applied electromagnetism.